The Role of Titanium in the Initiation of Localized Corrosion of Stainless Steel 444

S. M. Gateman[1], L. I. Stephens[1], S. C. Perry[1], R. Lacasse[2], R. Schulz[2], J. Mauzeroll[*1]

[1] Laboratory for Electrochemical Reactive Imaging and Detection of Biological Systems
McGill University, 801 Sherbrooke Street West, Montreal, QC, Canada, H3A 0B8
[2] Institut de recherche d'Hydro-Quebec 1800, boul. Lionel-Boulet, Varennes, QC, Canada J3X 1S1

*Corresponding Author:
Email: janine.mauzeroll@mcgill.ca
Phone: (+1) 514-398-3898

Table of Contents

1 Electrochemical experiments

1.1 Polarization curves

The corrosion cell chosen for extracting polarization curves from passivating metals (Figure S1) is of importance to minimize the unwanted formation of crevice corrosion. The bench top flat corrosion cell from Princeton Applied Research is unique due to its Teflon O-ring and reference electrode standard positioning system that ensures a standard surface area exposed and distance of the reference electrode from the working electrode respectively. The 3 electrode setup is completed with a Pt mesh employed as the counter electrode. The cell holds 300 mL of solution and comes together with four long screws holding all pieces in place with complementary O-rings. The electrodes are connected to the Biologic potentiostat and EC Lab software is used to interface with the electrochemical system.

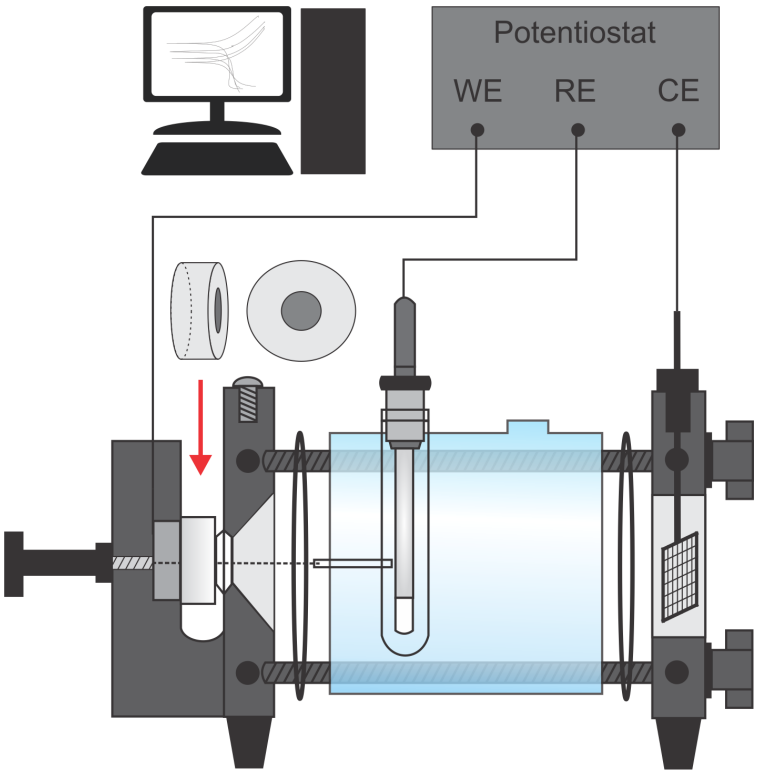

Figure S1: Schematic of the bench top corrosion cell used for all macroscopic electrochemical techniques.

1.1.1 Extraction of corrosion parameters from polarization curves

When the anodic and cathodic current densities are equal and the net current density approaches zero, the corresponding potential is referred to as the corrosion potential, E_{corr}, as illustrated in Figure S2. By extracting the intersection of the linear regions of cathodic and anodic branches the corrosion current density, j_{corr}, can be obtained.[1] However, due to the spontaneous passive film formation of the Fe/Cr alloy,[2] the anodic branch reaches a stable plateau known as the limiting current, or j_{lim}.

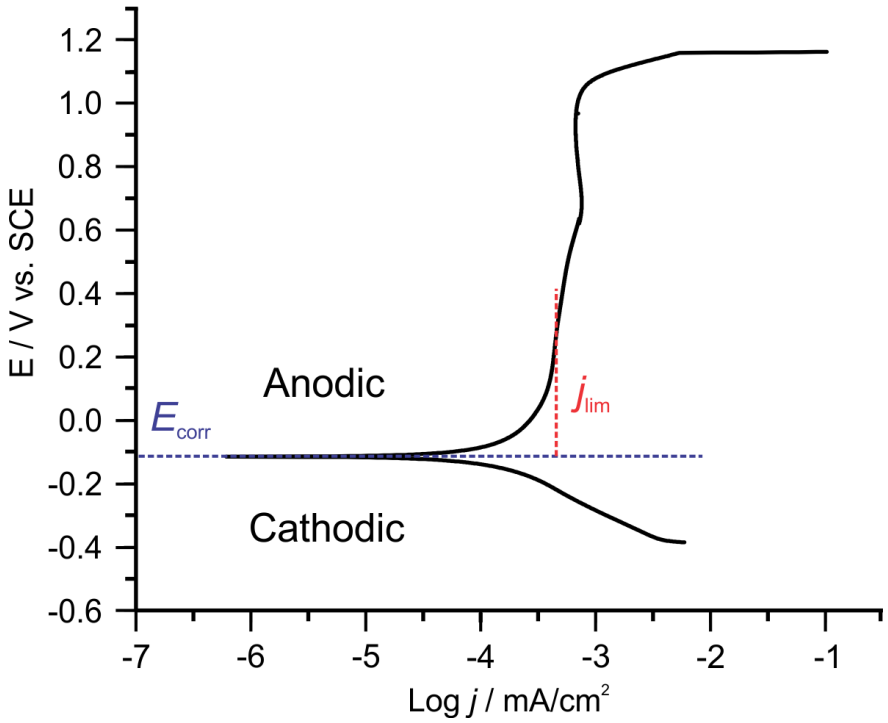

Figure S2: A typical polarization curve obtained from a prepared SS 444 sample showing the change from anodic to cathodic current through the E_{corr} and j_{lim} measured.

1.2 SECM

1.2.1 Carbon microelectrode (C-ME) fabrication procedure

A 4 μm diameter carbon fiber (HEKA, Germany) was attached to the end of a thin copper wire (0.5 mm diameter) using silver epoxy (EPO-TEK H20E; Epoxy Technology) and was cured at 120°C for 15 min. The Carbon fiber was threaded into a micropipette pulled using soda lime glass capillary (AR8350; L, 75 0.5 mm; o.d., 1.0 0.05 mm; i.d., 0.4267 0.05 mm; S, 0.2867 mm, Hilgenberg, GmbH) and a P-2000 micropipette puller using the previously reported pulling program.[3] The electroactive material was sealed inside the micropipette using a PC-10-CA vertical pipette puller and heating the C-ME tip for 8 s. The C-ME tip was reinforced with a borosilicate shell (L, 75 mm; o.d., 2.0 mm; i.d., 1.16 mm, Sutter Instruments) and soldered to a gold pin for easy electrochemical connection. The C-ME was polished with 0.05 μm alumina powder (Struers, Canada) and cleaned with acetone before each experiment.

1.2.2 Instrumentation

The popular mode of SECM in feedback requires the presence of an electrochemically active redox mediator to be present in solution.[4] When the UME is far from the substrate and in bulk solution, the flux of the redox mediator to the UME's surface is measured as a steady state current. As the tip of the UME is brought closer to the substrate, the diffusion of the redox mediator is hindered or enhanced depending on the electrical conductivity of the test specimen. Rastering the UME across an insulating surface gives a current map dependent purely on surface topography, whereas a map obtained over a conductive substrate would result in a signal with contributions from both topography and surface reactivity. A specimen with a heterogeneous microstructure could then be imaged using feedback mode to gather information about local reactivity on the material.

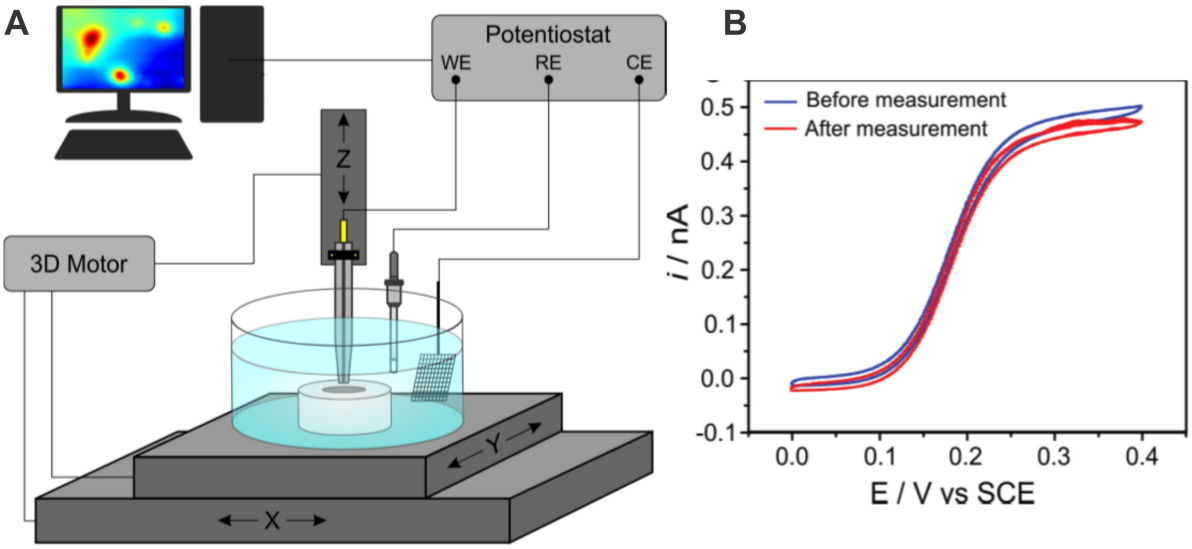

Figure S3: (A) A schematic of a typical SECM setup where the UME is positioned above the substrate using peizo electric motors as the working electrode within a three electrode setup. The UME working electrode can then be polarized at 350 mV vs. SCE in order to probe the reaction of the oxidation of FcMeOH. (B) Cyclic voltammograms of the C-ME in 1 mM FcMeOH 0.1 M KCl bulk solution at 10 mV/s before and after SECM measurements indicting the stability of the probes used in this study.

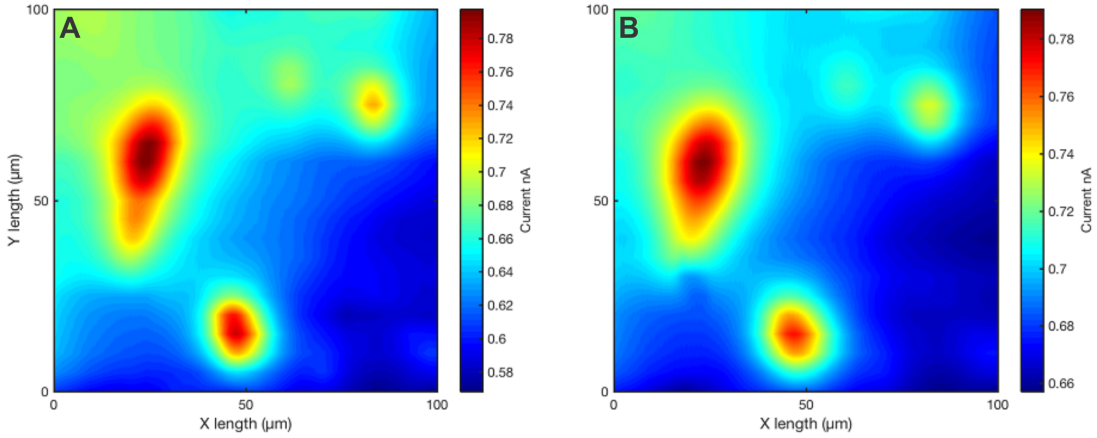

Figure S4: SECM current maps collected at the same area of the SS 444 substrate at 10 min (A) and 3 h (B) of immersion in the electrolyte. The little to no difference in the current maps after a few hours immersion demonstrates the TiN inclusions' ability to remain depassivated and exposed to the electrolyte as a vulnerable site.

2 Microstructural Characterization

2.1 ICP analysis of bulk alloy

Bulk quantitative analysis of the materials elemental composition was carried out using inductively coupled plasma optical emission spectroscopy (ICP-OES), using standard additions for calibration. The analysis was carried out on 3 samples with 3 replicates per sample. Table S1 compares the supplier's elemental composition claims to the experimental results. The quantity of C, Ti, Si and Nb could not be measured due to the need for corrosive acids such as HF for sample dissolution that irreversibly damage the glass nebulizer inside the instrument. Overall the experimental values are in agreement with the supplier's values.

Table S1: Verification of the elemental composition of the stainless steel given by the suppliers using experimental ICP-OES results. An asterisk indicates elements which could not be quantified in ICP-OES, for which the supplier's values have been given instead.

	Elemental composition of SS 444 (weight %)										
	Fe	Cr	Mo	Si	Ni	Nb	Mn	V	Cu	Ti	C
ArcelorMittal (Supplier)	79.9	17.07	1.89	0.17	0.24	0.307	0.28	0.11	0.063	0.15	0.02
Experimental ICP-OES	79.54	17.3	1.93	0.17*	0.25	0.307*	0.3	0.11	0.08	0.15*	0.02*

2.2 Additional microscopy

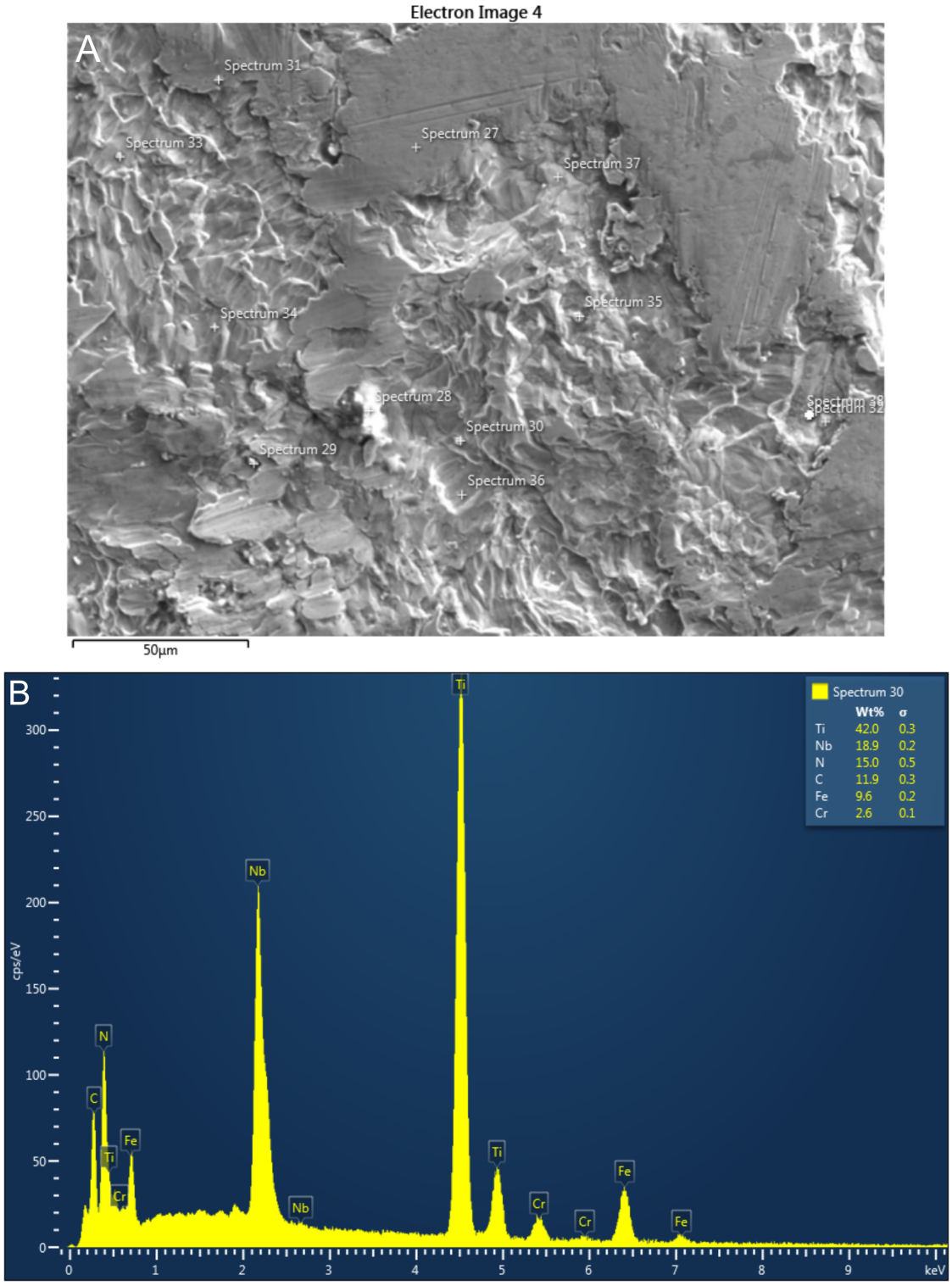

Figure S5: (A) SEM image of as received SS 444 samples and (B) EDX point analysis of a Ti rich inclusion.

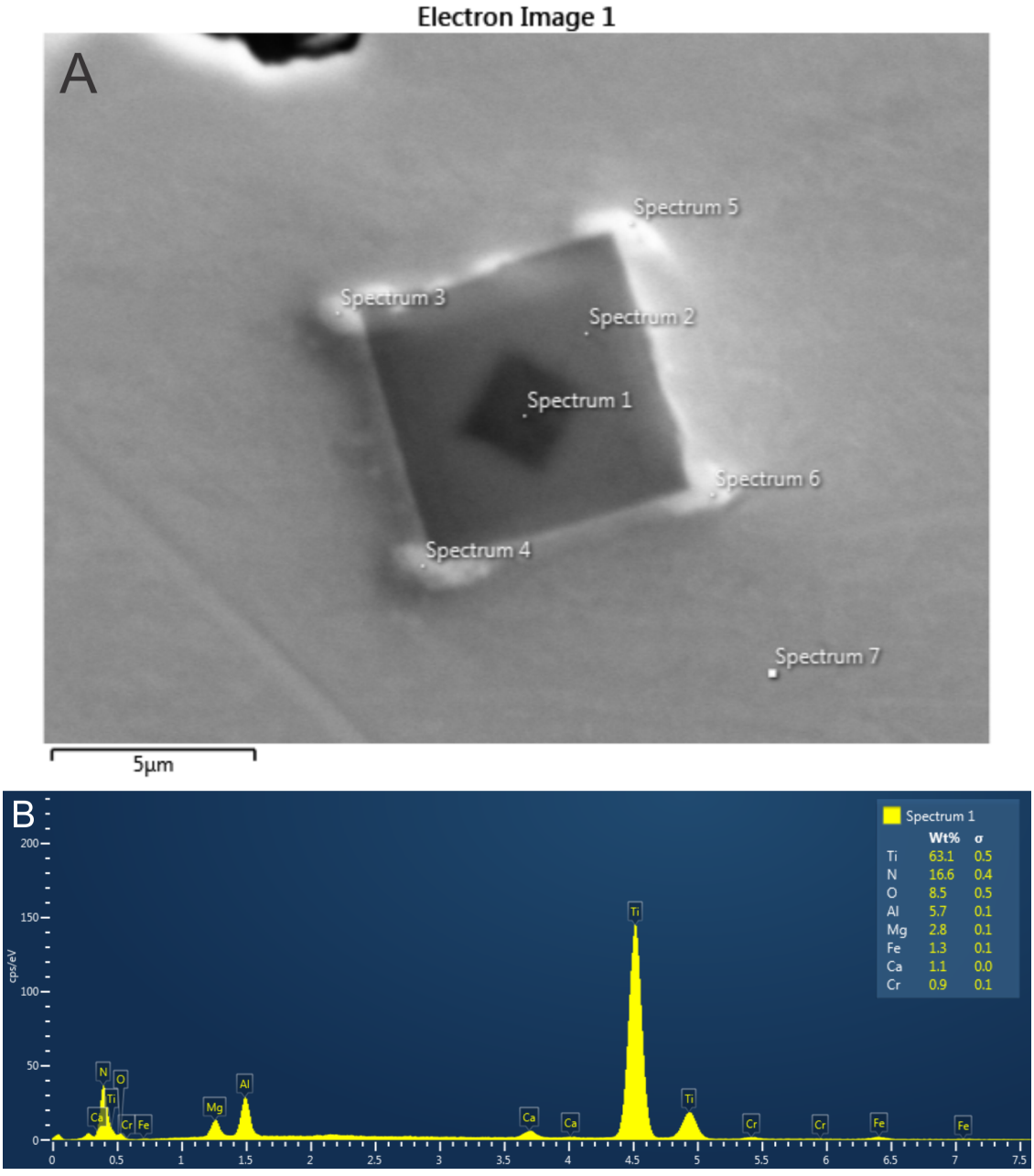

Figure S6: (A) SEM image of an oxide nucleated TiN inclusion and (B) corresponding EDX point analysis of the Mg and Al rich center.

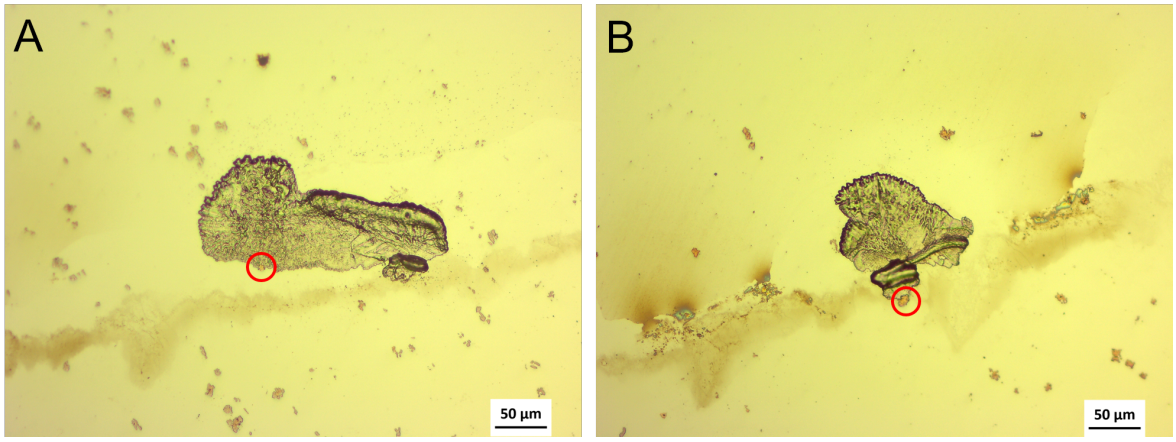

Figure S7: Micro crevice corrosion replicate tests indicating the presence of TiN inclusions in the middle/surrounding areas.

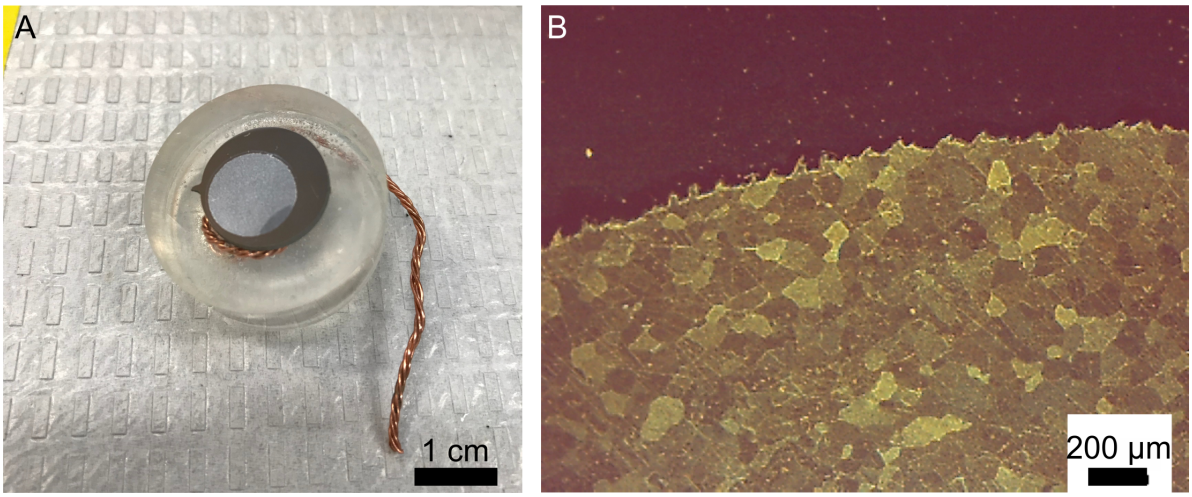

Figure S8: (A) Image of the SS 444 specimen after an etching experiment, showing the visible difference between polished and etched regions of the sample. (B) Optical micrograph taken at the interface between polished and etched sites on the sample, showing microstructural features exposed in etched areas.

3 Finite element simulations

3.1 Hardware requirements

All simulations were run using COMSOL Multiphysics 5.2 equipped with the Chemical Reaction Engineering Module on a machine running Windows 7 OS equipped with an octo-core Intel i7 processor and 16.0 GB of memory.

3.2 Fundamental model equations

Due to the square shape of the inclusion removing the axis of symmetry through the center of the UME employed in traditional finite element simulations,[5,6] a full 3D model was built. Approach curves were simulated using 'Transport of Diluted Species' physics with two species of interest: c_{ox} and c_{red}. The steady-state reaction rate for each tip-substrate distance probed was calculated according to the Nernst-Planck equation under conditions of no convection or migration:

$$\nabla \cdot (-D_i \nabla c_i) = R_i \tag{1}$$

Where D_i is the diffusion coefficient, c_i the concentration, and R_i the reaction rate of species i. It was assumed the oxidized and reduced species have the same diffusion coefficient, and therefore $D_{ox} = D_{red} = 7.7 \times 10^{-10}$ m^2/s.[7]

A schematic of the geometry (depicted in 2D for clarity, though a full 3D geometry was used for all simulations) is given in Figure S9. The radius of microelectrode (r_{UME}), radius of glass sheath (r_{glass}, where $R_g = r_{glass}/r_{UME}$), and diameter of inclusion (s) were chosen to match the dimensions determined from microscopy techniques with $r_{UME} = 2.35$ μm, $R_g = 9.6$ and $s = 8$ μm.

A probe approach curve (PAC) over the passive film was assumed to behave as a uniform substrate with normalized rate constant κ_p. A PAC over an inclusion was assumed to behave as a small conductive region with normalized rate constant κ_{in} in an otherwise uniform passive film.

Species are consumed and produced in accordance with the reactions at the surface descried by the following:

$$-n \cdot N_i = N_{0,j} \tag{2}$$

Where n is the normal vector, N_i is the flux of species i associated with mass transport, and $N_{0,i}$ is the flux of species i associated with a chemical reaction at the surface. The nature of $N_{0,i}$ is dependent on the nature of the reaction occurring at the surface. For example, the reactions

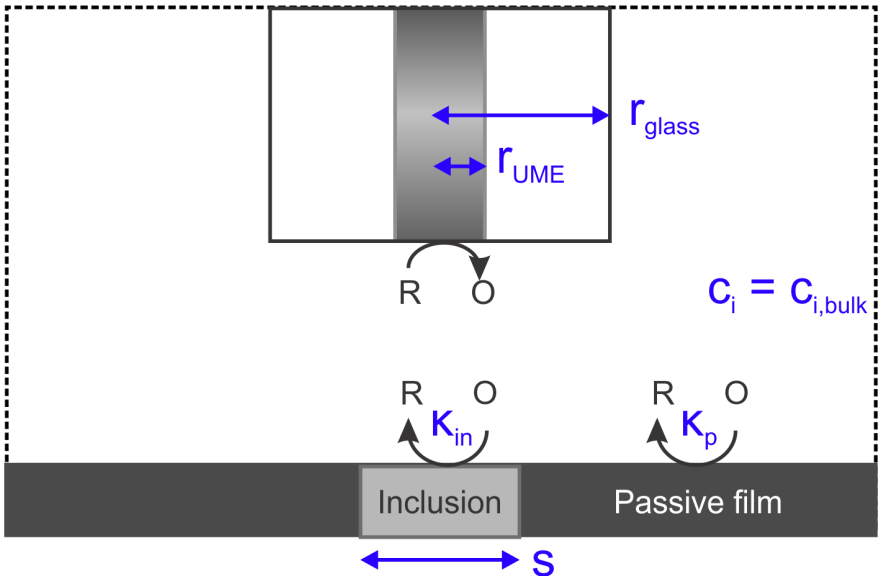

Figure S9: Schematic of the physics set-up employed in the simulation. Input simulation quantities are given in blue. The dashed line indicates the boundary condition where the local concentration was assumed equivalent to the bulk concentration. A condition of zero flux was set for all glass/electrolyte boundaries.

occurring at the inclusion are described by the following:

$$N_{0,c_{ox}} = -k_{in} c_{ox} \tag{3}$$

$$N_{0,c_{red}} = k_{in} c_{ox} \tag{4}$$

Where k_{in} is the rate constant over the inclusion.

In some cases, normalized quantities may be reported rather than the raw values. All distances are normalized to r_{UME}, all concentrations to the bulk concentration of reduced species, $c_{r,bulk}$ (where $c_{r,bulk} = 1$ mM and $c_{o,bulk} = 0$ mM), all currents to the steady state current in bulk solution, and rate constants such that:

$$\kappa = \frac{k r_{UME}}{D} \tag{5}$$

3.3 Geometry and mesh

The dimensions of the electrode and inclusion were chosen to match the probe used in the experiments, as given above. The electrolyte was represented as a hemispherical region centered on the UME with a radius of $100r_{UME}$.

A dense mesh with an element growth rate of 1.10 was introduced to the geometry with restrictions on maximum element size specified at the UME tip, inclusion surface, and glass sheath of $0.05r_{UME}$, $0.05s$, and $20.05r_{UME}$ respectively, for a final mesh consisting of approximately 650,000 finite elements. A sufficiently dense mesh and accurate model behavior was validated through comparison of simulated PAC over a uniform substrate to the existing analytical approximations,[8] as discussed in the following section.

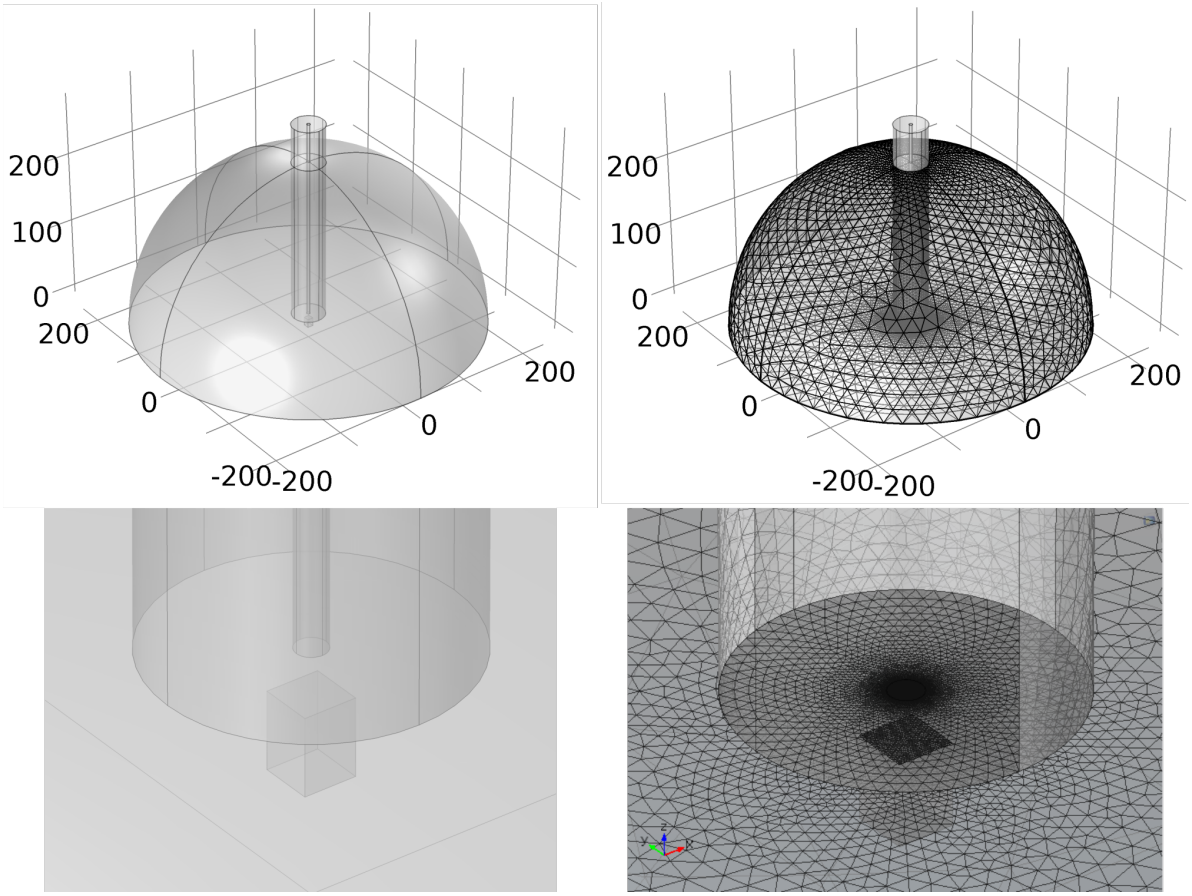

Figure S10: The geometry and mesh used for all simulations.

3.4 Validation

Accurate model behaviour was validated through comparison of simulated approach curves over a uniformly reacting surface to the analytical approximations for both pure feedback (Figure S11A) and mixed kinetics for a range of rate constants (Figure S11B).

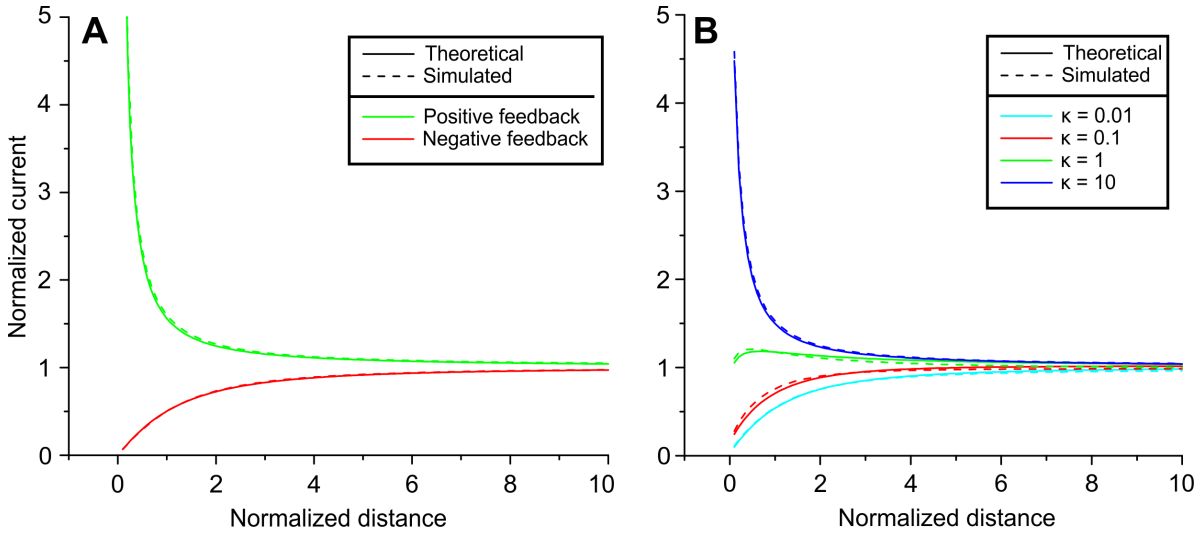

Figure S11: Validation of the model through comparison of simulated approach curves over a uniform substrate to the analytical approximations[8] for pure feedback (A) and mixed feedback (B).

3.5 Reproducibility

Three PAC using two different electrodes ($a_1 = 3.75$ μm and $Rg_1 = 2.78$, $a_2 = 2.35$ μm and $Rg_2 = 9.6$) were collected over the inclusion and passive film separately.

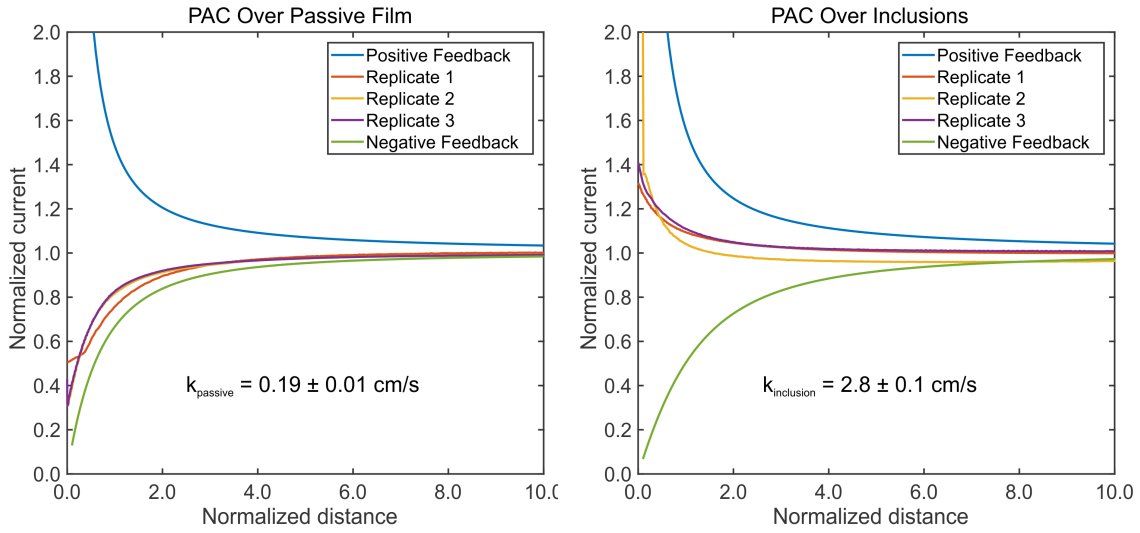

Figure S12: Comparison of all experimental PAC replicates collected over both the inclusion and passive film.

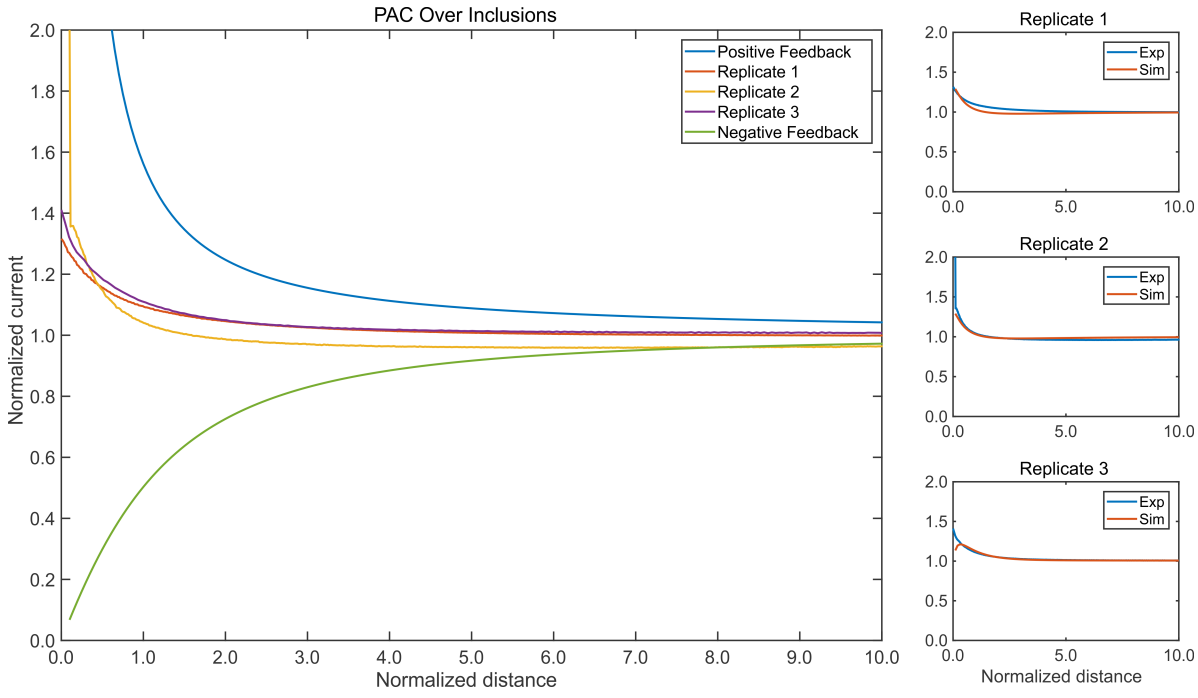

Figure S13: Experimental and simulation comparison for the three PAC performed over TiN inclusions.

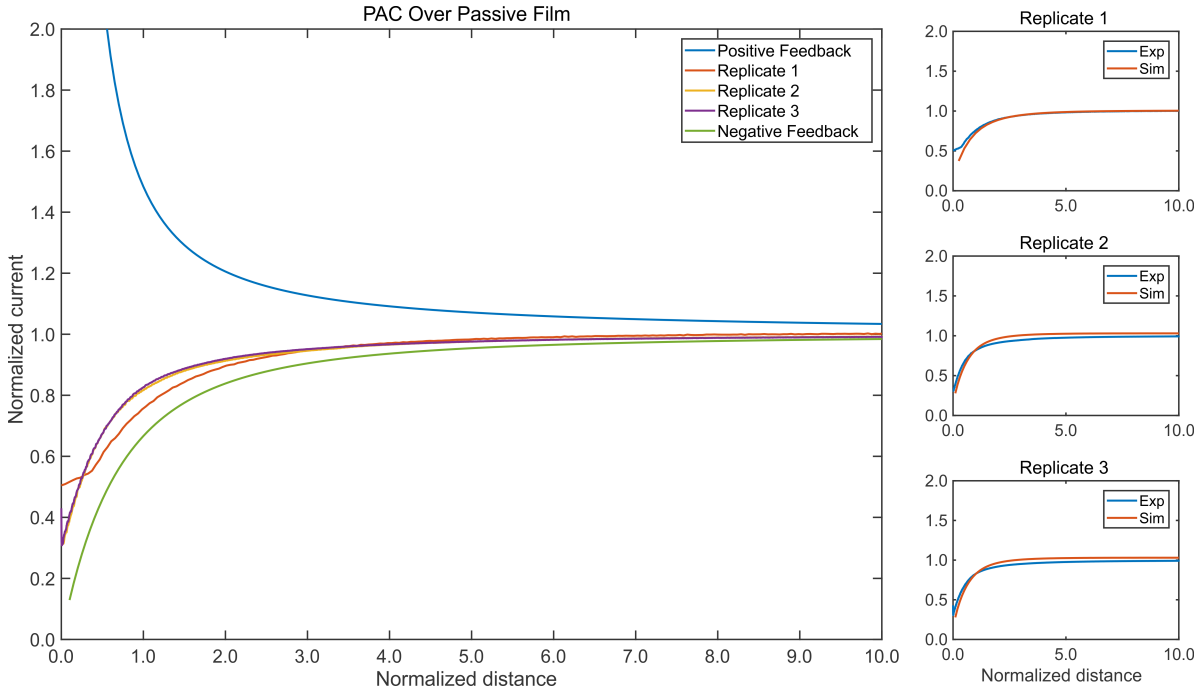

Figure S14: Experimental and simulation comparison for the three PAC performed over the passive film.

References

[1] Tait, W. S. *An introduction to electrochemical corrosion testing for practicing engineers and scientists*, 1st ed.; PairODocs Publications: Racine, WI, USA, 1994.

[2] Feliu, S.; Maffiotte, C.; Samaniego, A.; Galván, J. C.; Barranco, V. *Appl. Surf. Sci.* **2011**, *257*, 8558–8568.

[3] Danis, L.; Polcari, D.; Kwan, A.; Gateman, S. M.; Mauzeroll, J. *Anal. Chem.* **2015**, *87*, 2565–9.

[4] Kwak, J.; Bard, A. J. *Anal. Chem.* **1989**, *61*, 1221–1227.

[5] Zhu, R.; Qin, Z.; Noël, J. J.; Shoesmith, D. W.; Ding, Z. *Anal. Chem.* **2008**, *80*, 1437–1447.

[6] Jensen, M. B.; Guerard, A.; Tallman, D. E.; Bierwagen, G. P. *J. Electrochem. Soc.* **2008**, *155*, C324–C332.

[7] Anicet, N.; Bourdillon, C.; Moiroux, J.; Savéant, J.-M. *J. Phys. Chem. B* **1998**, *102*, 9844–9849.

[8] Lefrou, C.; Cornut, R. *ChemPhysChem* **2010**, *11*, 547–556.